






## RESEARCH ARTICLE

# Posttreatment of powder aerosol deposited oxide ceramic films by high power LED

Tobias Nazarenus<sup>1</sup>  | Kira Schlesier<sup>1</sup> | Simon Biberger<sup>2</sup> | Jörg Exner<sup>1</sup>  | Jaroslaw Kita<sup>1</sup>  | Anna Köhler<sup>2</sup>  | Ralf Moos<sup>1</sup> 

<sup>1</sup> Department of Functional Materials, University of Bayreuth, Universitaetsstrasse 30, Bayreuth 95447, Germany

<sup>2</sup> Soft Matter Optoelectronics, Bayreuth Institute of Macromolecular Research (BIMF) and Bavarian Polymer Institute (BPI), Department of Physics, University of Bayreuth, Universitaetsstrasse 30, Bayreuth 95447, Germany

## Correspondence

Tobias Nazarenus, Department of Functional Materials, University of Bayreuth, Universitätsstraße 30, Bayreuth D-95447, Germany.

Email: [functional.materials@uni-bayreuth.de](mailto:functional.materials@uni-bayreuth.de)

Anna Köhler, Soft Matter Optoelectronics, Bayreuth Institute of Macromolecular Research (BIMF) and Bavarian Polymer Institute (BPI), Department of Physics, University of Bayreuth, Universitätsstraße 30, Bayreuth D-95447, Germany.

Email: [anna.koehler@uni-bayreuth.de](mailto:anna.koehler@uni-bayreuth.de)

## Funding information

German Research Foundation, Grant/Award Numbers: MO-1060/37-1, KO 3973/2-1

## Abstract

The powder aerosol deposition (PAD) method is becoming increasingly important as an energetically advantageous coating method compared to classic ceramic technologies. However, due to the process-related lattice deformation, ceramic coatings often exhibit reduced functional properties in the as-deposited state. A thermal posttreatment at temperatures well below the sintering temperature can significantly reduce the lattice deformation and the stress within the film to restore the functional film properties close to sintered bulk samples. In this work, the optothermal posttreatment of PAD films using three different high-power light emitting diodes (HP-LED) with different wavelengths within the visible light spectrum is investigated as an alternative to time-consuming furnace or energy-intensive laser processes on the example of thermoelectric  $\text{CuFe}_{0.98}\text{Sn}_{0.02}\text{O}_2$  films. We demonstrate that the space-saving LED-based posttreatment not only restores the film properties but also significantly reduces the required processing time to a few seconds.

## KEYWORDS

$\text{CuFe}_{0.98}\text{Sn}_{0.02}\text{O}_2$ , efficient annealing, low temperature posttreatment, powder aerosol deposition (PAD) method, rapid processing

## 1 | INTRODUCTION

The powder aerosol deposition (PAD) method is a unique coating technology that enables the formation of dense ceramic films in the thickness range of  $0.5\ \mu\text{m}$  to  $100\ \mu\text{m}$  at room temperature (RT). During the moisture-free coating, sub-micron to micrometer-sized primary particles are accelerated from a fluidized bed onto a substrate by an applied pressure difference without further additives (e.g.,

organic binders).<sup>1</sup> The impact causes the particles to fracture along the grain boundaries and through the grains, creating unsaturated surfaces. Even if the exact mechanism of film formation has not been fully understood yet, the unsaturated fresh surfaces of the fractured particles seem to play an important role for the strong adhesion of the PAD film to the substrate. During the continuous impact of particles with high impact velocities of several hundred  $\text{m s}^{-1}$ , the nanocrystalline film growths and is

This is an open access article under the terms of the [Creative Commons Attribution](https://creativecommons.org/licenses/by/4.0/) License, which permits use, distribution and reproduction in any medium, provided the original work is properly cited.

© 2021 The Authors. *International Journal of Applied Ceramic Technology* published by Wiley Periodicals LLC on behalf of American Ceramics Society

densified by subsequently impacting particles according to the *hammering effect*.<sup>2,3</sup>

Due to the absence of thermal stress during the coating process, flexible and thermally less-stable substrates, such as polymers, can be coated, as well as metals, glasses, and dense or porous ceramics.<sup>4</sup> In addition, the coating materials do not exhibit thermally induced phase transformations. Owing to the high coating rates of up to  $2 \mu\text{m min}^{-1}$ , the industrial application of the technology, which has been under development since 1984, is becoming increasingly interesting.<sup>5,6</sup> Applications range from classic insulating protective films to functional films for sensor or photovoltaic applications to solid electrolytes for fuel cells or batteries.<sup>7,8</sup>

Although a film formation at RT has distinct advantages, the *Room Temperature Impact Consolidation* (RTIC) of the particles leads to atomic-scale lattice deformation, causes mechanical film stress, and reduces the charge carrier mobility and therefore lowers the electrical conductivity of functional films within the lattice.<sup>9,10</sup> Furthermore, the activation energy for charge carrier transport is increased in the as-deposited state.<sup>5</sup> And due to the deposition method also the magnetic properties of functional PAD films can be reduced compared to sintered bulk samples.<sup>11</sup> The nm-sized particles and pores can additionally influence the optical appearance of the films.<sup>12–14</sup>

To regain the full bulk-like functional film properties, a thermal posttreatment is necessary, where the disordered lattice relaxes.<sup>15</sup> As outlined in Figure 1, the ionic and/or electronic conductivity in the as-deposited state,  $\sigma_{\text{as-dep.}}$ , can significantly be reduced compared to sintered bulk samples (often by more than two to four orders of magnitude). At low temperatures, the heating process increases the conductivity due to a higher number of charge carriers within the distorted atomic lattice (region I).<sup>16</sup> When the temperature is increased further, the lattice relaxes as pointed out in Figure 1B. The higher lattice order increases the conductivity additionally (region II). After reaching a material-specific annealing temperature  $T_{\text{ann.}}$ , the lattice order is restored, and higher temperatures have no significant influence on the lattice anymore (region III). Exner et al. found that the annealing temperature  $T_{\text{ann.}}$  in general depends on the melting temperature  $T_{\text{mp}}$  of the material according to Equation (1) and is significantly below the sintering temperature.<sup>17</sup>

$$\frac{T_{\text{ann.}}}{K} = \frac{1}{6} \frac{T_{\text{mp}}}{K} + 730 \quad (1)$$

The remanent lattice restoration leads to a higher charge carrier mobility at lower temperatures during cooling (region IV). This way, post-annealing can lead to an increase in conductivity of the film. The temperature-dependent conductivity during any further heating process follows the cooling curve of the initial posttreatment. Due

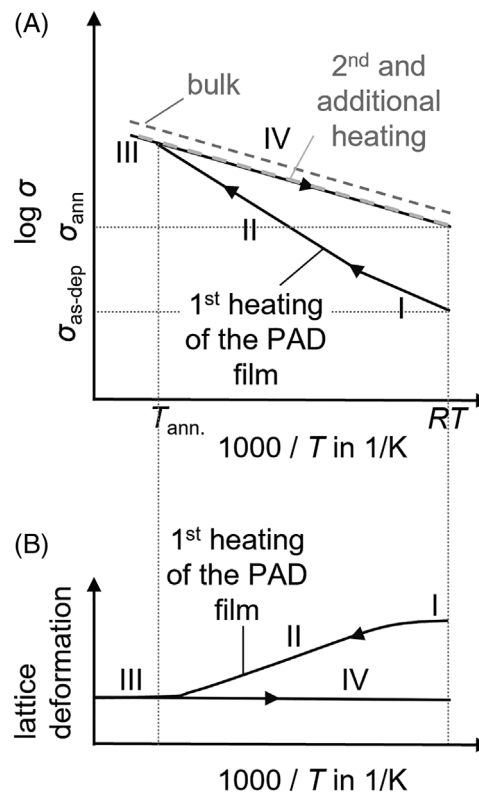


FIGURE 1 Schematic sketch on the influence of a thermal post-annealing on powder aerosol deposition (PAD) films regarding (A) the conductivity and (B) the lattice deformation

to the nanocrystalline microstructure of the film, the conductivity can be slightly reduced compared to bulk reference samples sintered at  $T > 1000^\circ\text{C}$ .

Although this posttreatment is conducted in furnaces at temperatures significantly below the sintering temperature of the coating material, the applied thermal stress may be challenging for temperature-sensitive substrates (like polymers) or may cause interdiffusion reactions between the coating material and the substrate that may negatively affect the functional properties.<sup>18</sup> As an alternative to the furnace-based annealing with low heating and cooling rates of approximate  $5 \text{ K min}^{-1}$ , laser irradiation allows for a rapid posttreatment with a local energy input. The thermal interaction depth of the laser irradiation and therefore the annealing depth strongly depend on the wavelength and the scan speed as well as on the laser beam profile (i.e., Gaussian beam profile or flat top beam profile).<sup>19–21</sup> Laser sources with a wavelength in the range of 400–700 nm are stated to be ideal for  $5 \mu\text{m}$  thick PAD films, depending on the material properties such as the band gap.<sup>22–24</sup>

To reduce both, the thermal stress caused by the post-treatment and long process times, this paper focuses on an inexpensive, rapid optothermal posttreatment of PAD films with a minimum required energy input. Therefore, three different high-power light emitting diodes (HP-LED) in the visible light spectrum (blue, green, and amber) are

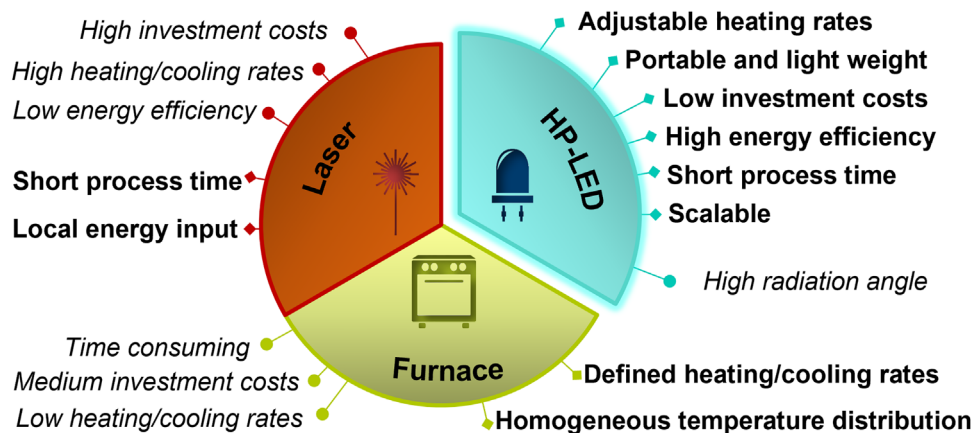


FIGURE 2 Comparison of different posttreatment methods and their individual advantages and disadvantages

used and further described according to their specifications in the experimental section. A comparison of the individual advantages and disadvantages of a laser-, a furnace- and an HP-LED-based posttreatment is shown in Figure 2. Electronically conducting thermoelectric  $\text{CuFe}_{0.98}\text{Sn}_{0.02}\text{O}_2$  films served as an exemplary material. For these films, a high electrical conductivity is required since they are intended to be used, for example, as p-type conductor in thermoelectric generators. Furthermore, the interaction between this film material and laser irradiation as well as a furnace-based posttreatment has been documented earlier, which allows for the comparison of the three methods.<sup>25,26</sup>

## 2 | EXPERIMENTAL

### 2.1 | Powder synthesis

The  $\text{CuFe}_{0.98}\text{Sn}_{0.02}\text{O}_2$  powder was synthesized via the mixed-oxide route. The precursor powders  $\text{Cu}_2\text{O}$  (Alpha Aesar, 99 % purity),  $\text{Fe}_2\text{O}_3$  (Alfa Aesar, 98 % purity), and  $\text{SnO}_2$  (Alfa Aesar, 99.9 % purity) were mixed stoichiometrically and milled in a planetary ball mill (Fritsch Pulverisette 5, Idar-Oberstein, Germany) with a zirconia milling jar ( $\text{ZrO}_2$ , stabilized with 3.5 wt%  $\text{MgO}$ ) with zirconia milling balls ( $\text{ZrO}_2$ , stabilized with  $\text{Y}_2\text{O}_3$ ) and cyclohexane serving as milling fluid for 4 h. After the homogenization milling, cyclohexane was removed in a rotary evaporator (Heidolph Instruments, Schwabach, Germany). The powder was calcined at  $1050^\circ\text{C}$  on quartz glass in a tube furnace (Carbolite, Neuhaus, Germany) with 1%  $\text{O}_2$  in nitrogen atmosphere for 12 h. For a process-suitable particle size, the powders were milled, followed by a drying and sieving step with  $90\ \mu\text{m}$  meshes. The powders were stored at  $200^\circ\text{C}$  in laboratory atmosphere before they were used for PAD. Additional details can be found in previous publications.<sup>26,27</sup>

### 2.2 | Film fabrication via PAD

For the deposition, a custom build PAD apparatus as described by Hanft et al. was used.<sup>1</sup> A vacuum pump (consisting of a rotary and a booster pump) evacuates the deposition chamber to 1 mbar and the aerosol generating unit to  $\sim 250$  mbar during operation. With an oxygen flow rate of  $6\ \text{L}\ \text{min}^{-1}$ , an aerosol is transported from the fluidized powder bed in the aerosol generation unit to the deposition chamber. By the pressure difference between the aerosol generation unit and the deposition chamber, the aerosol is accelerated through a slit nozzle (orifice size:  $10 \times 0.5\ \text{mm}^2$ ) onto the substrates in the deposition chamber. The powders were deposited on alumina substrates (Rubalit 708S, CeramTec, Marktreidwitz, Germany) with screen-printed platinum interdigital electrodes (IDE) and on screen-printed gold-platinum thermocouples, both schematically shown in Figure 3. The substrates were placed onto a horizontally moveable ( $5\ \text{mm}\ \text{s}^{-1}$ ) substrate holder distanced 2 mm from the nozzle.

### 2.3 | Film posttreatment via high power LED

The custom-built setup shown in Figure 4 is used for the post-deposition annealing of the  $\text{CuFe}_{0.98}\text{Sn}_{0.02}\text{O}_2$  PAD films via HP-LED. The downward facing HP-LED is located within an aluminum container and directly attached to the ceiling of the upper half-shell using thermal paste for heat dissipation. Samples are placed within a height-adjustable sample holder directly below the LED. The HP-LEDs are operated by a software controllable power supply (EA-PSI 5040-40 A, EA Elektro-Automatik GmbH & Co. KG, Viersen, Germany), both connected by an electrical feed-through connector. Three different types

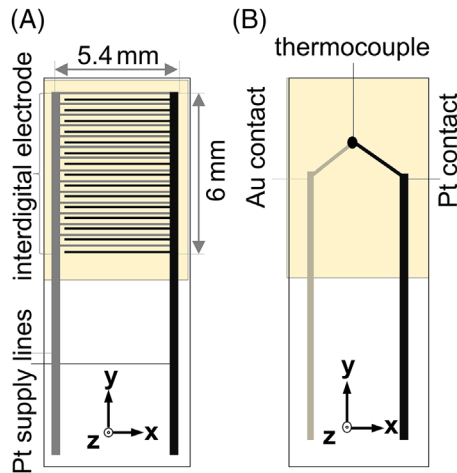


**FIGURE 3** Alumina substrates with (A) screen-printed platinum interdigital electrodes and (B) screen-printed gold-platinum thermocouples. The deposition area is additionally colored as a guide for the eye

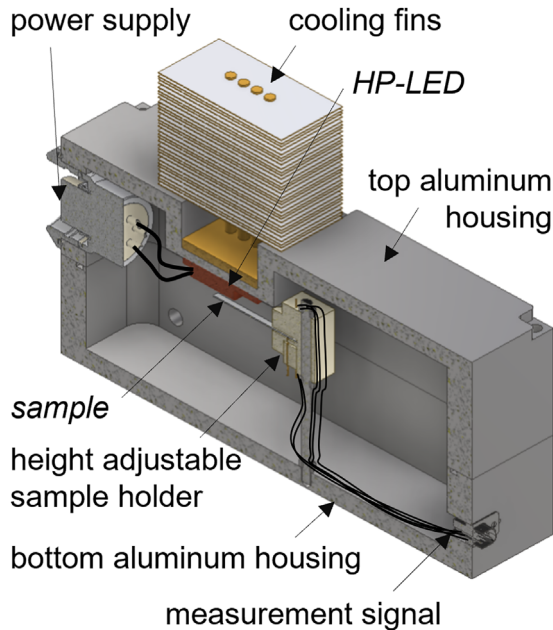


**FIGURE 4** Half-section model of the custom-built apparatus for post-deposition annealing of powder aerosol deposition (PAD) films via high-power light emitting diode (HP-LED)

of LED have been used: a blue LED (LE B P3W 01), a green LED (LE CG P3A 01), and an amber LED (LE A P3W 01), all of the “projection series” of OSRAM Opto Semiconductors Inc., Germany.

A separate signal-port in the lower half-shell allows for continuously measuring the temperature via thermocouples and the film conductivity via the IDE as described in Figure 3 by a Novocontrol  $\alpha$ -Analyzer (Novocontrol Technologies, Montabaur, Germany). For the electrical measurements, platinum wires connect the sample and

signal-port in the aluminum half-shell. According to Equation (2), the conductivity  $\sigma_{\text{eff}}$  of the film is calculated based on the film resistance  $R_{\text{tot}}$  and the IDE geometry  $F$  (PAD film thickness  $t$ , finger length  $l = 4.5$  mm, finger spacing  $d = 100 \mu\text{m}$ , electrode width  $w = 100 \mu\text{m}$ , and number of fingers on each electrode side  $m = 15$ ).<sup>28</sup>

$$\sigma_{\text{eff}} = \frac{1}{R_{\text{tot}} \cdot F} = \frac{d}{R_{\text{tot}} \cdot [(2m - 1) \cdot l \cdot t + 2m \cdot w \cdot t]} \quad (2)$$

To determine the substrate temperature, gold and platinum contacts (cf. Figure 3B) are connected to the gold and platinum wires, respectively, of the signal-port feed-through. By additionally measuring the temperature at the junction with a PT100 temperature sensor, the temperature of the thermocouple at the interface between the film and the substrate can be calculated based on the thermopower-induced voltage according to Equation (3) for voltages up to  $1952 \mu\text{V}$  and Equation (4) for voltages between  $1953 \mu\text{V}$  and  $17085 \mu\text{V}$ .<sup>29</sup> Here, the thermoelectric voltage  $U_{\text{therm}}$  is the sum of the measured signal voltage  $U_{\text{signal}}$  and the thermoelectric voltage at the reference junction  $U_{\text{therm.ref}}$ . The additional thermoelectric voltage  $U_{\text{therm.ref}}$  considers the reference temperature at the junction when the platinum and gold wire are connected to copper wires and are calculated according to Equation (6). The variables  $b_i$  and  $a_i$  are listed in the supporting information.

$$\frac{T}{^\circ\text{C}} = \sum_{i=0}^8 b_i \cdot \left( \frac{U_{\text{therm}}}{\mu\text{V}} \right)^i \quad (3)$$

$$\frac{T}{^\circ\text{C}} = \sum_{i=0}^{11} b_i \cdot \left( \frac{U_{\text{therm}}/\mu\text{V} - 9645}{7620} \right)^i \quad (4)$$

$$U_{\text{therm}} = U_{\text{signal}} + U_{\text{therm.ref}} \quad (5)$$

$$\frac{U_{\text{therm.ref}}(T)}{\mu\text{V}} = \sum_{i=0}^n a_i \cdot \left( \frac{T}{^\circ\text{C}} \right)^i \quad (6)$$

Two different HP-LED operation modes were used during the posttreatment experiments. Figure 5 depicts the scheme of the test runs.

- In one mode, the applied current  $I_{\text{LED}}$  was varied in 1 A steps between 1 A and 30 A. Exposure times of 2 min were selected, interrupted by pauses between each step of 15 min to allow for complete cooling to RT, as illustrated in Figure 5A. In addition, to investigate the

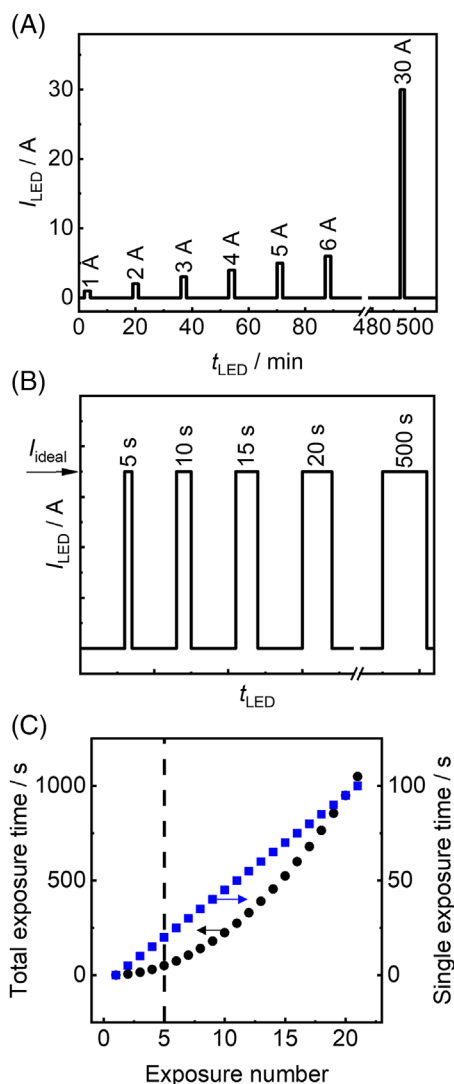


**FIGURE 5** High-power light emitting diode (HP-LED) operating modes: (A) constant exposure time of 2 min with varying current from 1 A to 30 A in 1 A steps, (B) constant current with increasing exposure time per step, (C) single and total exposure time for each exposure number in (B) (different time scales)

influence of the power density, three different distances (4 mm, 14 mm, and 40 mm) between LEDs and PAD film were chosen. This operation mode enables to determine the ideal LED current, respectively LED power, during the posttreatment for a maximized film conductivity.

- In another mode, the exposure time was varied according to Figure 5B between 5 s and 500 s, while each additional exposure time-step after pauses of 2 min was increased by 5 s. Thus, a sample after the fifth exposure-step was exposed to the longest single exposure time of 25 s, whereas the total LED irradiation duration adds up to 75 s (sum of all previous exposure times). During the complete second LED operation mode, the wavelength-dependent, ideal LED current and the previously deter-

mined power and working distance between LED and PAD surface were set. In Figure 5C, the longest single and total radiation exposure times are shown for each used posttreatment step in Figure 5B.

## 2.4 | Optical LED characterization

In order to characterize the spectral output of the employed HP-LED, the light of the LED was guided via a glass fiber and analyzed by a MS 125 spectrograph (Oriel Instruments). The resulting spectrum was recorded by a CCD camera (Andor DU420A-OE) and spectrally corrected. Neutral density filters were used in front of the glass fiber to uniformly attenuate the light intensity in order to prevent oversaturation of the sensor of the CCD-camera sensor. The radiation intensity  $\Phi$  of each of the HP-LED was measured with a thermopile sensor (PM10V1, Coherent) with a sensitivity range between 0.25 and  $3 \mu\text{m}$  in combination with a power meter (Fieldmate, Coherent) in different distances to the HP-LED.

## 2.5 | Mechanical and optical film analysis

The film thicknesses were determined by a profile stylus instrument (Perthometer P4, Mahr, Göttingen, Germany). The optical film morphology was analyzed by scanning electron microscope (Zeiss Leo Gemini 1530 VP; field emission cathode, inlens and secondary electron detector, operating voltage 3 kV). In order to determine the absorbance of the films, reflectance and transmittance spectra were collected on a Cary 5000 UV-VIS spectrometer by Varian, equipped with an integrating sphere. The wavelength-dependent absorbance  $A(\lambda)$  was then calculated according to Equation (7) as a function of the transmission  $T(\lambda)$  and the reflection  $R(\lambda)$ .

$$A(\lambda) = 1 - T(\lambda) - R(\lambda) \quad (7)$$

## 3 | RESULTS AND DISCUSSION

### 3.1 | Optical film properties

To define the influence of the LED irradiation on the nanocrystalline  $\text{CuFe}_{0.98}\text{Sn}_{0.02}\text{O}_2$  films, the absorbance of the films was measured by recording the transmittance and reflectance spectrum with an integrating sphere. The data are plotted in a Tauc representation (Figure 6A). It correlates the squared product of the absorption coefficient  $\alpha$ , the photon energy  $h\nu$  with the incoming

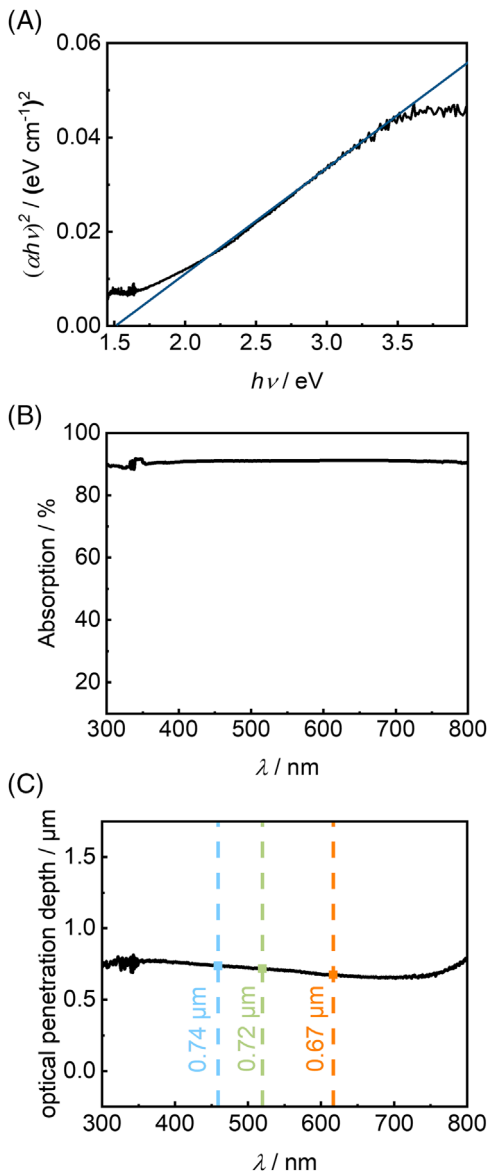


**FIGURE 6** Optical film properties of  $\text{CuFe}_{0.98}\text{Sn}_{0.02}\text{O}_2$ : (A) Tauc plot, (B) wavelength-dependent absorption of the powder aerosol deposition (PAD) film, (C) wavelength-dependent optical penetration depth. The mean wavelengths of the applied light emitting diode (LED) are indicated by vertical dashed lines

photon energy shown as the product of Planck's constant and the wavelength. The bandgap of the film can be determined by applying a straight line on the slope of the plot, where the intersection with the x-axis defines the exact value.<sup>30,31</sup> Compared with the bandgap of sintered bulk samples ( $E_{g,\text{bulk}} = 1.3$  eV), a slightly increased bandgap of  $E_{g,\text{PAD film}} = 1.5$  eV is calculated with this method for PAD films in the as-deposited state.<sup>32,33</sup> Considering the accuracy of the measurement method, the measured data agree well with literature.<sup>34</sup> Since for effective optical absorption, the photon energy must be higher than the band gap, an emission source with a maximum wavelength of 826 nm

can be tolerated. Figure 6B shows the percentage absorption of the PAD film depending on the wavelength in the optical region from 300 nm to 800 nm, calculated according to Equation (7). Since the required wavelength is below 800 nm, a high percentage of the radiation is absorbed. Furthermore, the absorption of 90% is nearly constant over the wavelength region. In Figure 6C, the dependency of the optical penetration depth  $l_{\text{optical}}$  on the wavelength in the range from 300 nm to 800 nm is shown based on Equation (8) with the absorption coefficient  $\alpha$ , the film thickness  $t$  and the optical measurement data from Figure 6B.<sup>35</sup>

$$l_{\text{optical}} = \frac{1}{\alpha} = \frac{1}{\frac{1}{t} \ln \left[ \frac{(1-R)^2}{2T} + \left\{ \frac{(1-R)^4}{4T^2} + R^2 \right\}^{\frac{1}{2}} \right]} \quad (8)$$

As a guide for the eye, the peak wavelengths of the three different LEDs (blue, green, and amber) are inserted. Since the absorption coefficient is almost independent on the wavelength, no significant changes can be observed for the optical penetration depth. Thus, at a depth of 700 nm, the intensity of the electromagnetic wave is already reduced to  $1/e$  ( $\sim 36.8\%$ ) of the incoming surface intensity. This indicates that only the top film surface of a several micrometer thick PAD film is directly affected by the selected HP-LED radiation, which agrees well with the results on study of laser-based annealing of  $\text{CuFe}_{0.98}\text{Sn}_{0.02}\text{O}_2$  PAD films.<sup>25</sup> The calculations point out an inhomogeneous temperature profile along the z-axis of the film for very short annealing times. On the other hand, a homogeneous temperature distribution can be expected for films in the  $\mu\text{m}$ -range when they are exposed to irradiation for several minutes.

### 3.2 | Optical LED power characteristics

As mentioned in the experimental section, the LED power characteristics are measured by a CCD-camera in combination with a spectrograph. In Figure 7A, the number of counts is plotted against the wavelength for all three used LED (blue, green, and amber) at different applied LED currents (1 A, 5 A, and 10 A). While the blue and amber LED emit photons in a comparatively narrow wavelength range from 415 nm to 500 nm with a maximum at 459 nm and from 590 nm to 650 nm with a maximum at 617 nm, respectively, the green LED emits in a wide wavelength range showing three local maxima at 429 nm, 540 nm, and 710 nm. However, the largest number of photons is emitted between 480 nm and 630 nm. By increasing the applied current  $I_{\text{LED}}$ , the number of counts (and therefore number of photons) increases without a shift in the emitted wavelength spectra.

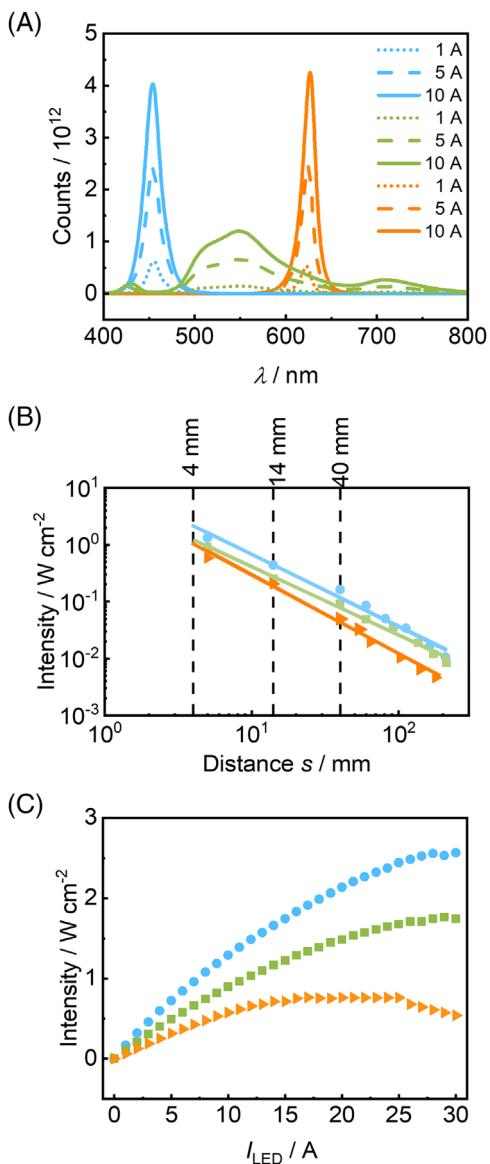


**FIGURE 7** Characteristics of the three used high-power light emitting diode (LED) (blue: dot, green: square, orange: triangle): (A) LED emission spectra as a function of the applied current, (B) radiation intensity in dependency on the distances between LED and powder aerosol deposition (PAD) film ( $I_{\text{LED}} = 10$  A), the measurement points are connected as a guide for the eye, and (C) radiation intensity in dependency on the applied current at a working distance of 4 mm

The dependency of the working distance between the LED and the sensor (respectively the PAD film) on the emitted radiation intensity  $\Phi$  for defined LED currents is measured by a thermophile sensor. All LEDs are operated with a current of 10 A. The data are plotted in Figure 7B.

Since the LEDs have a high radiation angle of  $120^\circ$ , the working distance influences the intensity. As the working distances 4 mm and 14 mm play a major role in the annealing experiments (see below), they are additionally

marked. Since the minimum adjustable distance for the characterization is 5 mm, the measured data are additionally extrapolated down to 4 mm. The amber LED reaches up to  $0.59 \text{ W cm}^{-2}$ , whereas for the blue LED a more than doubled value of  $1.30 \text{ W cm}^{-2}$  is found at the lowest measured working distance of 5 mm. The green LED reaches  $0.90 \text{ mW cm}^{-2}$  at 5 mm working distance. For high working distances ( $>40$  mm), the difference in the radiation intensity decreases significantly.

Furthermore, the distance between LED and the radiation intensity sensor is held constant at 4-mm distance while the LED current is varied between 0 A and 30 A in 1 A steps. By increasing the applied current, the radiation intensity increases and asymptotically approaches to defined values for the three different LED. For the blue LED, a maximum radiation intensity of  $2.5 \text{ W cm}^{-2}$  is reached at  $I_{\text{LED}} = 30$  A, whereas the green and the amber LED exhibit  $1.7 \text{ W cm}^{-2}$  at  $I_{\text{LED}} = 29$  A and  $0.7 \text{ W cm}^{-2}$  at  $I_{\text{LED}} = 25$  A, respectively.

### 3.3 | Thermal effect of radiation

Low distances between the radiation source (the LED) and the sample can also result in a significant temperature increase of the PAD film and the substrate. The thermal effect of the LED radiation on the film temperature is measured by thermocouples as described earlier (see Figure 3B). The PAD-coated thermocouples were exposed to the three HP-LED at different heights according to Figure 5A. In Figure 8, the temperature at the interface between the PAD film and the alumina substrate is shown depending on the applied LED current  $I_{\text{LED}}$ . The closer the LED is placed to the film, the higher is the interface temperature. These results are consistent with Figure 7, since the radiation intensity significantly increases with decreasing working distance due to the high radiation angle of  $120^\circ$  of the LEDs. The shorter the wavelength, the higher the photon energy and therefore the maximum temperature. Consequently, the same annealing temperature is reached at different applied currents  $I_{\text{LED}}$ . The blue ( $\lambda_{\text{blue}} = 459$  nm) and the green ( $\lambda_{\text{green}} = 520$  nm) LED reach the maximum interface temperature of  $T_{\text{max, blue}} = 430^\circ\text{C}$  and  $T_{\text{max, green}} = 328^\circ\text{C}$ , respectively, at the minimum distance (4 mm) and maximum applied LED current  $I_{\text{LED}}$  of 30 A. In contrast, the amber ( $\lambda_{\text{amber}} = 617$  nm) LED reaches a maximum interface temperature of  $T_{\text{max, amber}} = 138^\circ\text{C}$  at  $I_{\text{LED}} = 22$  A. At higher distances, the maximum temperature is significantly reduced. Due to the shown correlation between the radiation intensity and the applied LED current in Figure 7C, the resulting temperature for the different LEDs can additionally be calculated as a function of the

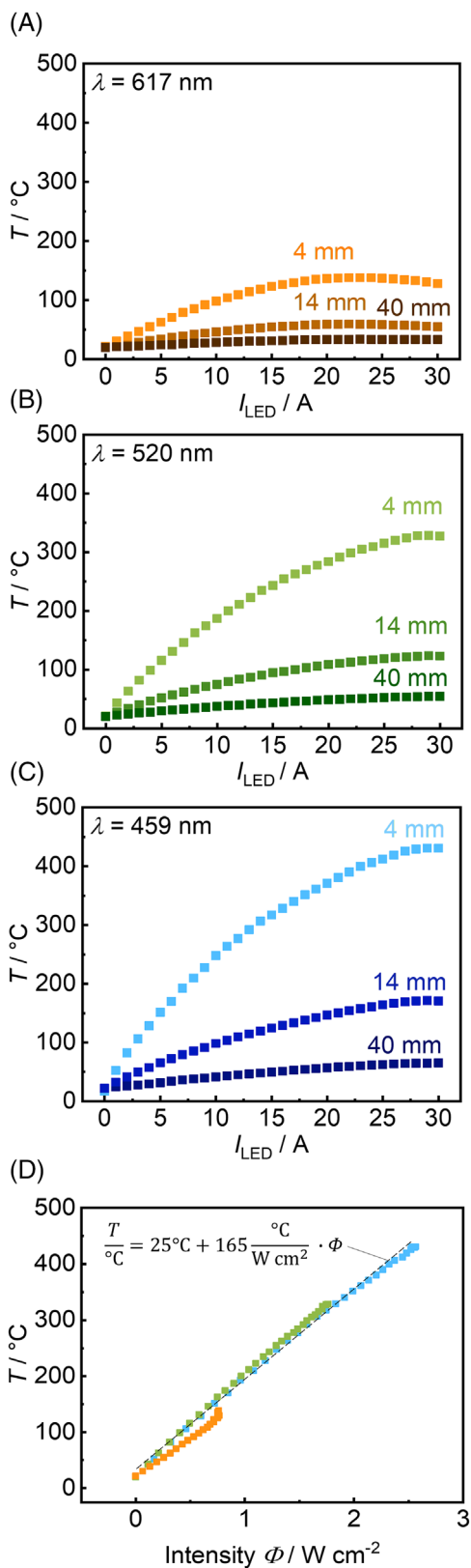


**FIGURE 8** Current-dependent substrate surface temperature for different light emitting diode (LED) at defined working distances of 4 mm, 14 mm, and 40 mm: (A) amber LED, (B) green LED, (C) blue LED, and (D) correlation between the intensity of all three LED and the temperature at a fixed working distance of 4 mm. The linear correlation is added in (D) as a guide for the eye

radiation intensity in Figure 8D. The hysteresis for the amber HP-LED at high applied current results from a reduced emission intensity, which can also be found in Figure 7C.

### 3.4 | Influence of the LED radiation on PAD films

To analyze the effect of LED irradiation on the functional PAD film properties, in particular the electronic conductivity, IDEs were coated with  $\text{CuFe}_{0.98}\text{Sn}_{0.02}\text{O}_2$  and exposed to radiation according to Figure 5A. During the complete posttreatment, the conductivity of the PAD film  $\sigma_{\text{film}}$  was measured. The *operando* posttreatment process is exemplarily plotted for the green LED at 4 mm working distance in Figure 9. In addition to the applied current  $I_{\text{LED}}$ , the resulting power  $P_{\text{LED}}$ , and the film conductivity  $\sigma_{\text{film}}$ , and the calculated interface temperature  $T_{\text{surface}}$  between substrate and film based on the results from Figure 8 are shown. Since the surface temperature is calculated based on the applied current from Figure 8, the heating process cannot be displayed.

During exposure, the film conductivity increases due to two reasons. First, the number of charge carriers increases due to photon absorption caused by the low band gap of 1.5 eV as discussed previously. Second, the increased temperature leads to a permanent conductivity increase since the previously stressed lattice relaxes as explained in the introduction. Since the last effect is remanent, it can be seen at RT after LED irradiation. During the *operando* conductivity determination, after each exposure time of 2 min, the 15 min pauses were sufficient to cool the PAD film to RT. As can also be seen in exemplarily detail for an applied current of  $I_{\text{LED}} = 6 \text{ A}$  in Figure 9B, the increase in  $I_{\text{LED}}$  up to 10 A leads to a permanent conductivity increase. This partial increase with each exposure step adds up to a total of over two decades from  $10^{-6} \text{ S cm}^{-1}$  to  $10^{-4} \text{ S cm}^{-1}$ . The remanent positive effect of a posttreatment has also been found for different film materials.<sup>17</sup> Already at 7 A, the calculated film conductivity reaches  $3.8 \cdot 10^{-2} \text{ S cm}^{-1}$  during irradiation. While the RT conductivity can be exactly measured using the present setup, the maximum detectable conductivity during exposure is limited by the two-wire IDE including the used sample holder. For highly conductive films, the resistance of the platinum electrodes and connecting cables dominate the electrical measurement, creating the impression of a saturated conductivity level during LED irradiation.

In the magnification example of Figure 9, a reduction in the permanent film conductivity at RT occurs for high  $I_{\text{LED}} > 10 \text{ A}$ . This can be explained by a phase transformation from the  $\text{CuFeO}_2$  phase to  $\text{CuO}$  in oxygen rich



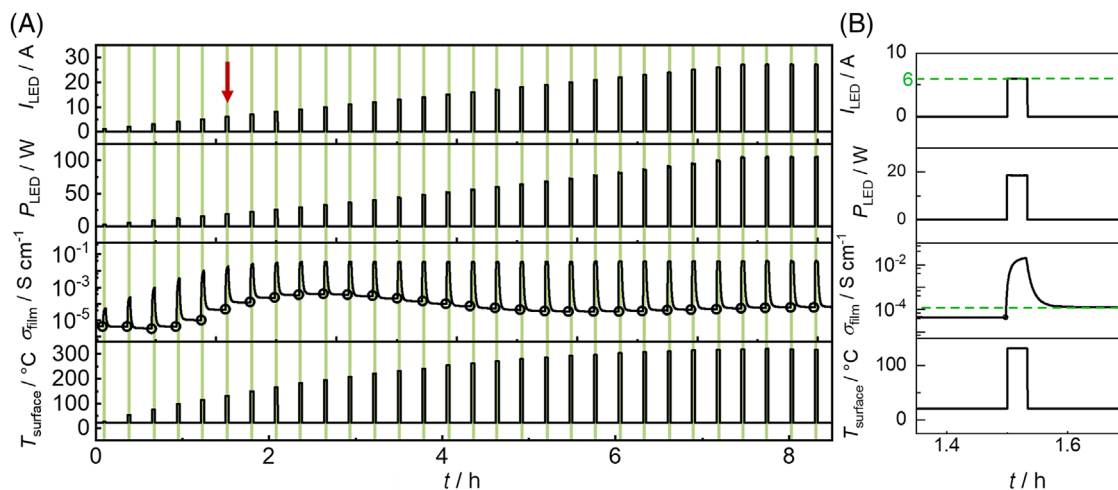
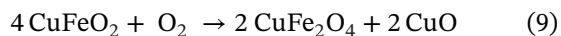


**FIGURE 9** (A) Measurement records: Effect of increasing the high-power light emitting diode (HP-LED) current on the film conductivity on the example of a green LED with a defined exposure time of 2 min as well as on the surface temperature based on the data of Figure 7. The green lines indicate the operation of the LED as a guide for the eye. The red arrow indicates the application with 6 A, which is exemplarily magnified in (B). The permanent increase in conductivity  $\sigma_{\text{film}}$  is obvious. The circles indicate the conductivity data used for the following figures

atmosphere taking place at elevated temperatures according Equation (9).<sup>36</sup>



The same measurement protocol, which is shown exemplary in Figure 9, was applied for all three HP-LED and at all three defined heights (4 mm, 14 mm, and 40 mm). In Figure 10A-C, the permanent conductivity values at RT are plotted against the applied LED current  $I_{\text{LED}}$ . Please note the low deviation in the film conductivity in the as-deposited state of all samples, demonstrating a high and uniform coating quality. Since the positive effect on the conductivity seems to be based on the temperature, it follows the expectation that higher distances lead to a lower increase. With exception of the blue LED, already at 14 mm distance no increase in conductivity can be observed anymore. Although the qualitative correlation between film conductivity and the applied LED currents remains constant for Figure 10A-C, the comparison between the three different LEDs shows that the higher the LED wavelength is, the higher must be the applied current to reach the maximum conductivity. The post-deposition annealing with the amber LED requires 15 A, the green LED 11 A, and the blue LED 7 A. After a minor decrease of  $\sigma_{\text{RT}}$  for the lowest applied current  $I_{\text{LED}}$ , the conductivity generally increases by two orders of magnitude from approximate  $2 \cdot 10^{-6} \text{ S cm}^{-1}$  to  $3 \cdot 10^{-4} \text{ S cm}^{-1}$ . When applying too high LED currents, a phase transformation occurs under laboratory annealing atmosphere in presence of oxygen and humidity as previously discussed.<sup>36</sup>

In general, the applied current results in an LED-dependent intensity  $\Phi$  as described earlier. When normalizing the optical output power of the LED, it becomes apparent that the rise in electronic conductivity of the PAD film directly depends on the intensity as shown in Figure 10D. Nearly independent of the LED wavelength, a maximum conductivity is reached when an intensity of  $0.75 \pm 0.05 \text{ W cm}^{-2}$  is applied. Since all LED wavelengths are equally absorbed (Figure 6C), the emitted LED radiation intensity, and hence the resulting temperature, turns out to be the key parameter. Already at temperatures significantly below  $200^\circ\text{C}$ , the optothermal posttreatment results in a conductivity increase caused by lattice relaxation without sintering and grain growth.

Since the effect that a thermal posttreatment leads to a lattice relaxation and therefore to an increase in film conductivity is well documented in literature, the XRD patterns are not shown in detail.

### 3.5 | Optimized LED exposure time

After having investigated the influence of LED irradiation on  $\text{CuFe}_{0.98}\text{Sn}_{0.02}\text{O}_2$  films with respect to power densities, the influence of the exposure time was investigated. The results are shown in Figure 11. The exposure duration was varied according to Figure 5B (5 s, 10 s, 15 s, 20 s...) with the ideal current  $I_{\text{LED}}$  extracted from Figure 10. Already after the 30 s exposure duration step with the blue LED, a maximum film conductivity of  $3.4 \cdot 10^{-4} \text{ S cm}^{-1}$  was found. In addition, an exposure time of up to 1 min is also sufficient for a complete posttreatment to restore bulk-like

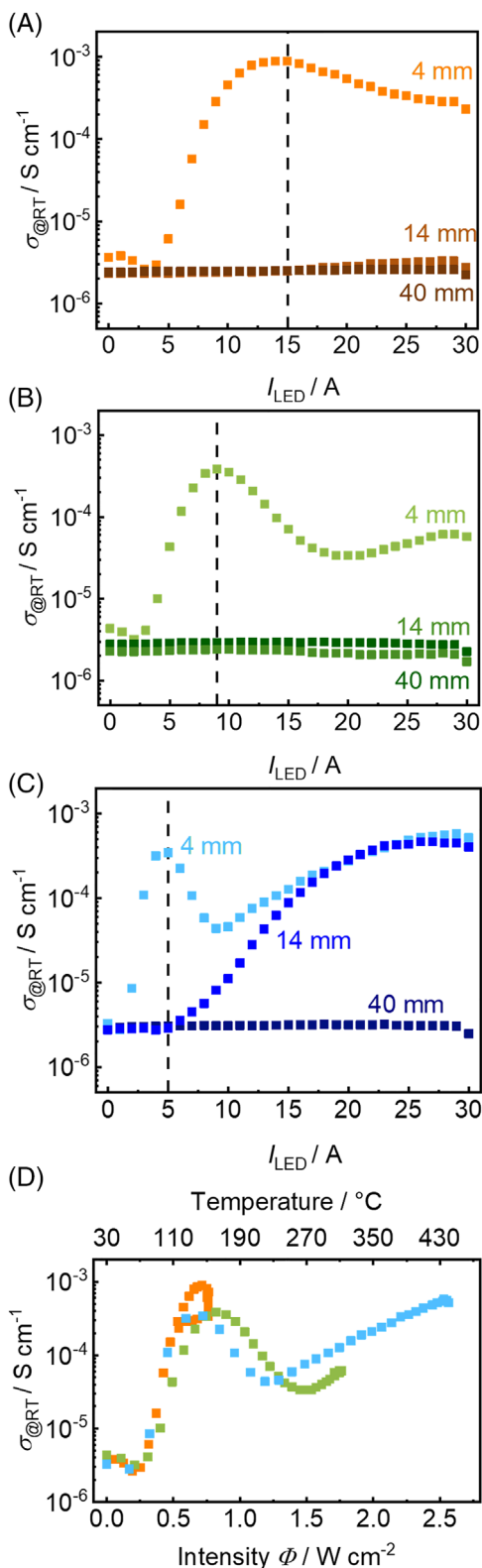


**FIGURE 10** Current-dependent conductivity of  $\text{CuFe}_{0.98}\text{Sn}_{0.02}\text{O}_2$  samples when irradiated by different light emitting diode (LED) at defined distances of 4 mm, 14 mm, and 40 mm: (A) amber LED, (B) green LED, and (C) blue LED. The current for the maximum conductivity is marked by a vertical-dashed line as a guide for the eye. Additionally, (D) the conductivity is shown for each HP-LED at a working distance of 4 mm as a function of the radiation intensity  $\Phi$  and the temperature according to Figure 8D

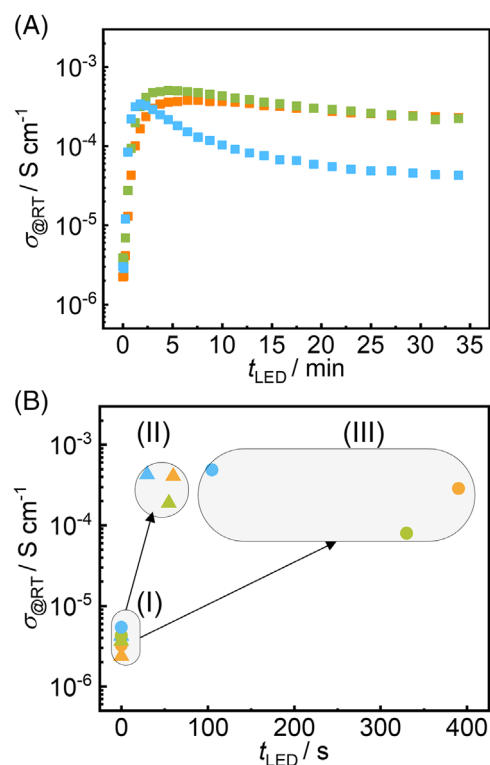


**FIGURE 11** Correlation between the room temperature film conductivity  $\sigma_{\text{RT}}$  and the exposure time  $t_{\text{LED}}$  when the optimum light emitting diode (LED) current is applied at a distance of 4 mm: (A) film conductivity for increasing exposure intervals according to Figure 4B, (B) comparison between the film conductivity in the as-deposited state (I), a single exposure with the ideal exposure time for maximum conductivity (II), and a single exposure with the total exposure time (III)

conductivity film properties for the two additional LEDs ( $t_{\text{LED, green}} = 55 \text{ s}$ ,  $t_{\text{LED, amber}} = 60 \text{ s}$ ). To disprove the hypothesis that also the previous, shorter exposure times, affect the conductivity increase, additionally one film was exposed according to the above-found parameters as shown in Figure 11B. Also, for an increase of the exposure time that includes the mentioned previous single exposures, no additional increase in the conductivity can be found. As an example, the two films with a conductivity of  $5.0 \cdot 10^{-6} \text{ S cm}^{-1}$  in the as-deposited state were annealed in a single step for 30 s and for 105 s. The difference in the conductivity between the short time annealing ( $\sigma_{\text{blue LED, 30s}} = 4.2 \cdot 10^{-4} \text{ S cm}^{-1}$ ) and the long-time annealing ( $\sigma_{\text{blue LED, 105s}} = 4.8 \cdot 10^{-4} \text{ S cm}^{-1}$ ) is small. The conducted dwell time optimization results in a significant process time reduction from 2 min to 30 s. The rapid optothermal posttreatment of the films is an additional advantage of the PAD film fabrication compared to long-lasting sintering processes.<sup>37</sup>

TABLE 1 Ideal parameter values for the three high-power light emitting diodes (HP-LEDs) in constant wave (cw) operation mode

LED	Current I/A	Distance s/mm	Temperature T/°C	Time $t_{LED}/s$	Conductivity $\sigma_{as-depo}/S\ cm^{-1}$	Conductivity $\sigma_{annealed}/S\ cm^{-1}$
Amber ( $\lambda = 617\ nm$ )	15	4	140	60	$5.0 \cdot 10^{-6}$	$4.0 \cdot 10^{-4}$
Green ( $\lambda = 520\ nm$ )	11	4	180	55	$5.0 \cdot 10^{-6}$	$1.9 \cdot 10^{-4}$
Blue ( $\lambda = 459\ nm$ )	7	4	180	30	$5.0 \cdot 10^{-6}$	$4.2 \cdot 10^{-4}$

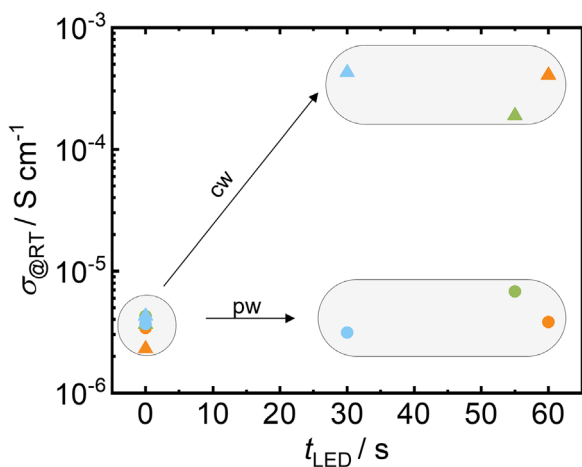


FIGURE 12 Conductivities before and after the pulsed (1 s pulses with 5 s break) and continuous operation of the light emitting diodes (LEDs) with 4-mm distance and the ideal LED current according to Table 1

### 3.6 | Operation modes

In addition to the described operation modes in Figure 5A,B, the software-based LED control enables a pulsed wave (pw) operation mode in contrast to the before-used constant wave (cw) operation mode. The effect of both modes on the conductivity behavior was analyzed. The already known ideal parameters for the working distance and the total duration were applied (summed up in Table 1) for that purpose. During the pw operation mode, after each exposition step of 1 s, a pause of 5 s was applied. In total, the films were exposed for the same duration.

In Figure 12, the impact of the different operation modes on the film conductivity is shown. It can be clearly stated that the operation mode has a significant influence on the film properties. While the cw mode leads to the described increase of the conductivity by approximately two decades, the pw mode has little to no impact on the conductivity. The data demonstrate that the effect is not due to the optical transition itself but rather due to the dissipation of the optically acquired energy as heat. Depending on the thermal conductivity of the sample, the exposure time needs to be long enough for the irradiation to cause an increase in the film temperature. This leads to a per-

manent reduction of the film stress and thus to a permanent increase in film conductivity. Due to the low irradiation power compared to a laser, an efficient posttreatment effect cannot be achieved by short single light pulses with LED.

### 3.7 | Film microstructure

Since the LED provide a local energy input in the PAD film, changes in the surface microstructure may occur. Figure 13 compares the surface (1) in the as-deposited state with the surface after the LED-based posttreatment with (2) amber, (3) blue, and (4) green light. All images show the typical bombardment crater structure that results from the continuous particle impact during the film formation according the RTIC mechanism. There is no evidence for the assumption that a different posttreatment effect occurs within the film compared to the furnace processing, as it has been demonstrated in contrast for a laser-based posttreatment.<sup>25</sup> There, due to the high locally induced energy density of laser irradiation, melting can easily occur. Although the LED radiation is sufficient for a posttreatment of PAD films, the effect differs from the laser-based posttreatment. Since the applied currents only lead to moderate temperature increase, the permanent increase in conductivity is not caused by grain growth. Consequently, the annealing effect is with very high probability caused by lattice stress relaxation.

## 4 | CONCLUSION

The PAD is a unique coating technique to produce ceramic films of several micrometer thickness at RT with high deposition rates. Based on the hard mechanical particle impact, atomic lattice deformations are generated within the film. They reduce the charge carrier mobility and therefore negatively affect the film properties.

By a thermal posttreatment, for example, in the furnace, the lattice may relax, and the electrical film properties are restored. However, a process in a furnace is time-consuming due to low heating and cooling rates.

In this study, we investigated a rapid, inexpensive, and scalable LED-based annealing process.

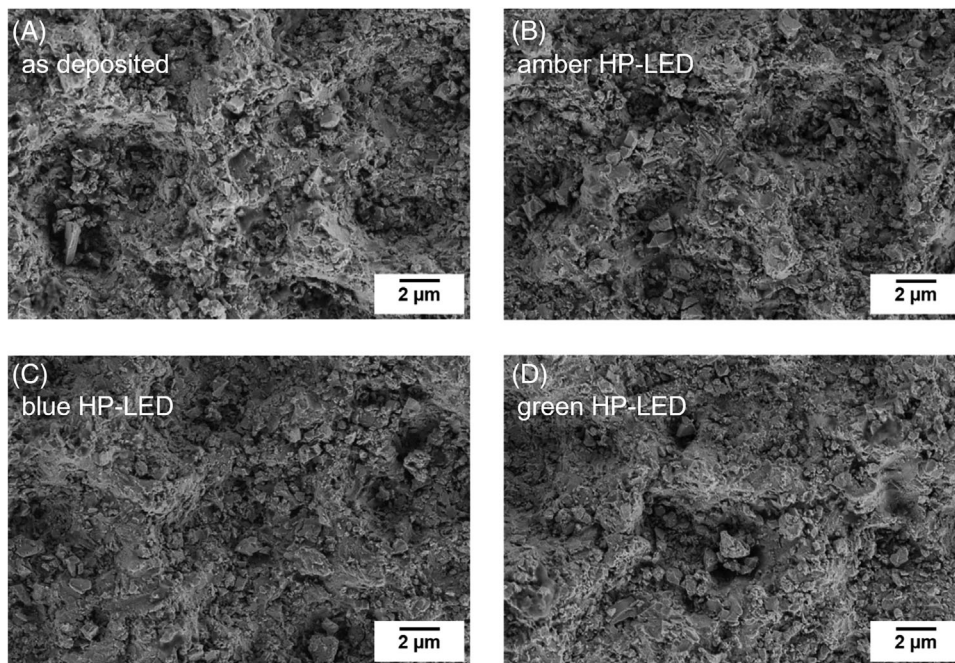


**FIGURE 13** SEM top-view images of the surface structure of  $\text{CuFe}_{0.98}\text{Sn}_{0.02}\text{O}_2$  PAD films (A) before an light emitting diode (LED) posttreatment, (B) after a posttreatment with amber LED, (C) after a posttreatment with blue LED, and (D) after a posttreatment with green LED. The posttreatment was conducted according to the parameters in Table 1

Thermoelectric  $\text{CuFe}_{0.98}\text{Sn}_{0.02}\text{O}_2$  films served as an example. This optothermal posttreatment was conducted in a custom-built setup, and the influence of the HP-LED radiation on the film conductivity was investigated in detail.

In comparison with the state-of-the-art posttreatment in a furnace, the duration can significantly be reduced from 1 h to less than 1 min. By the optothermal posttreatment, the conductivity of the PAD film can be increased from  $5.0 \cdot 10^{-6} \text{ S cm}^{-1}$  in the as-deposited state to up to  $4.8 \cdot 10^{-4} \text{ S cm}^{-1}$  using optimized LED posttreatment parameters, which is very close to bulk-values.

Due to the low optical penetration depth and the negligible influence of the irradiation in the pw operation mode, it can be concluded that the annealing effect is the result of an LED irradiation induced temperature increase, which causes a permanent lattice relaxation. However, the surface microstructure is not affected thereby. Since the energy input can be controlled easily and the annealing duration is significantly reduced with this method, it may even allow the post-deposition treatment of more temperature sensitive films or substrates. This way, temperature-based degradation processes and unintended interdiffusion reactions between the film and the substrate can be reduced or even avoided.

Although the calculation of the radiant intensity of the LED as well as the temperature measurements of the substrate-film-interface during the short process time and the conductivity increase of the PAD films expands the knowledge of what happens during the optothermal post-

treatment, the required energy to restore the lattice cannot be exactly given. Further studies may quantify this, which would allow for a deeper understanding of the deposition mechanism and resulting lattice distortions.

#### ACKNOWLEDGMENT

The authors would like to acknowledge the funding from the German Research Foundation (DFG, grant MO-1060/37-1 and grant KO 3973/2-1). They are indebted to Dr. Julian Kahle from the Chair for Soft Matter Optoelectronics in the Department of Physics for helpful hints during the optical measurements and furthermore, thank Mrs. Angelika Mergner and the Bavarian Polymer Institute (BPI) for SEM images.

Open access funding enabled and organized by Projekt DEAL.

#### CONFLICT OF INTEREST

The authors declare that there is no conflict of interest that could be perceived as prejudicing the impartiality of the research reported.

#### ORCID

Tobias Nazarenus  <https://orcid.org/0000-0002-0420-8373>

Jörg Exner  <https://orcid.org/0000-0002-1601-2968>

Jaroslav Kita  <https://orcid.org/0000-0001-7063-9828>

Anna Köhler  <https://orcid.org/0000-0001-5029-4420>

Ralf Moos  <https://orcid.org/0000-0001-7622-0120>

## REFERENCES

- Hanft D, Exner J, Schubert M, Stöcker T, Fuierer P, Moos R. An overview of the aerosol deposition method: process fundamentals and new trends in materials applications. *J. Ceram. Sci. Tech.* 2015;6:147–82.
- Akedo J. Room temperature impact consolidation and application to ceramic coatings: aerosol deposition method. *J. Ceram. Soc.* 2020;128:101–16.
- Lebedev M, Akedo J, Mori K, Eijū T. Simple self-selective method of velocity measurement for particles in impact-based deposition. *J. Vac. Sci. Technol. A.* 2000;18:563–6.
- Exner J, Nazarenus T, Kita J, Moos R. Dense Y-doped ion conducting perovskite films of BaZrO<sub>3</sub>, BaSnO<sub>3</sub>, and BaCeO<sub>3</sub> for SOFC applications produced by powder aerosol deposition at room temperature. *Int. J. Hydrog. Energy.* 2020;45:10000–10016. <https://doi.org/10.1016/j.ijhydene.2020.01.164>
- Nazarenus T, Sun Y, Exner J, Kita J, Moos R. Powder aerosol deposition as a method to produce garnet-type solid ceramic electrolytes: a study on electrochemical film properties and industrial application. *Energy Technol.* 2021;9(6):2100211. <https://doi.org/10.1002/ENTE.202100211>
- Kashu S, Fuchita E, Manabe T, Hayashi C. Deposition of ultra fine particles using a gas jet. *Jpn. J. Appl. Phys.* 1984;23:910–2.
- Schubert M, Hanft D, Nazarenus T, Exner J, Schubert M, Nieke P, et al. Powder aerosol deposition method — novel applications in the field of sensing and energy technology. *Funct. Mater. Lett.* 2019;12:1930005.
- Panzer F, Hanft D, Gujar TP, Kahle F-J, Thelakkat M, Köhler A, et al. Compact layers of hybrid halide perovskites fabricated via the aerosol deposition process-uncoupling material synthesis and layer formation. *Materials* 2016;9:277.
- Akedo J. Temperature impact consolidation (RTIC) of fine ceramic powder by aerosol deposition method and applications to microdevices. *J. Therm. Spray. Tech.* 2008;17:181–98. <https://doi.org/10.1007/s11666-008-9163-7>
- Baba S, Huang L, Sato H, Funahashi R, Akedo J. Room-temperature fast deposition and characterization of nanocrystalline Bi<sub>0.4</sub>Sb<sub>1.6</sub>Te<sub>3</sub> thick films by aerosol deposition. *J. Phys. Conf. Ser.* 2012;379:12011. <https://doi.org/10.1088/1742-6596/379/1/012011>
- Kagotani T, Kobayashi R, Sugimoto S, Inomata K, Okayama K, Akedo J. Magnetic properties and microwave characteristics of Ni–Zn–Cu ferrite film fabricated by aerosol deposition method. *J Magn Magn Mater.* 2005;290–291:1442–5.
- Nakada M, Ohashi K, Akedo J. Electro-optic properties of Pb(Zr<sub>1-x</sub>Ti<sub>x</sub>)O<sub>3</sub> (X = 0, 0.3, 0.6) films prepared by aerosol deposition. *Jpn. J. Appl. Phys.* 2005;44:L1088–90.
- Nakada M, Ohashi K, Akedo J. Electro-optical properties and structures of (Pb, La)(Zr, Ti)O<sub>3</sub> and PbTiO<sub>3</sub> films prepared using aerosol deposition method *Jpn. J. Appl. Phys.* 2004;43: 6543–8.
- Kim H, Kim K, Choi D, Lee M, Chu W-S, Ahn S-H, et al. Microstructural control of the electrochromic and ion storage layers on the performance of an electrochromic device fabricated by the kinetic spray technique. *Int. J. of Precis. Eng. Manuf.-Green Tech.* 2018;5:231–8. <https://doi.org/10.1007/s40684-018-0023-8>
- Hanft D, Exner J, Moos R. Thick-films of garnet-type lithium ion conductor prepared by the aerosol deposition method: the role of morphology and annealing treatment on the ionic conductivity. *J. Pow. Sour.* 2017;361:61–9.
- Nozaki T, Hayashi K, Kajitani T. Thermoelectric properties of delafossite-type oxide CuFe<sub>1-x</sub>Ni<sub>x</sub>O<sub>2</sub> (0 < x < 0.05). *J. Chem. Eng. Japan.* 2007;40:1205–9. <https://doi.org/10.1252/jcej.07WE146>
- Exner J, Nazarenus T, Hanft D, Kita J, Moos R. What happens during thermal post-treatment of powder aerosol deposited functional ceramic films? Explanations based on an experiment-enhanced literature survey. *Adv. Mater.* 2020;32:1908104.
- Baba S, Sato H, Huang L, Uritani A, Funahashi R, Akedo J. Formation and characterization of polyethylene terephthalate-based (Bi<sub>0.15</sub>Sb<sub>0.85</sub>)<sub>2</sub>Te<sub>3</sub> thermoelectric modules with CoSb<sub>3</sub> adhesion layer by aerosol deposition. *J. Alloys Compd.* 2014;589:56–60. <https://doi.org/10.1016/j.jallcom.2013.11.180>
- Baba S, Akedo J. Fiber laser annealing of nanocrystalline PZT thick film prepared by aerosol deposition. *Appl. Surf. Sci.* 2009;255:9791–5.
- Baba S, Akedo J. Damage-free and short annealing of Pb(Zr,Ti)O<sub>3</sub> thick films directly deposited on stainless steel sheet by aerosol deposition with CO<sub>2</sub> laser radiation. *J. Am. Ceram. Soc.* 2005;88:1407–10.
- Palneedi H, Park JH, Maurya D, Peddigari M, Hwang G-T, Annapureddy V, et al. Unleashing the full potential of magnetoelectric coupling in film heterostructures. *Adv. Mater.* 2018;30:1870094. <https://doi.org/10.1002/adma.201605688>
- Palneedi H, Maurya D, Kim G-Y, Annapureddy V, Noh M-S, Kang C-Y, et al. Unleashing the full potential of magnetoelectric coupling in film heterostructures. *Adv. Mater.* 2017;29:1605688.
- Patil DR, Annapureddy V, Kaarthik J, Thakre A, Akedo J, Ryu J. Piezoelectric thick film deposition via powder/granule spray in vacuum: a review. *Actuators* 2020;9:59. <https://doi.org/10.3390/act9030059>
- Palneedi H, Maurya D, Geng LD, Song H-C, Hwang G-T, Peddigari M, et al. Enhanced self-biased magnetoelectric coupling in laser-annealed Pb(Zr,Ti)O<sub>3</sub> thick film deposited on Ni Foil. *ACS Appl. Mater. Interfaces.* 2018;10:11018–25. <https://doi.org/10.1021/acsami.7b16706>
- Nazarenus T, Kita J, Moos R, Exner J. Laser-annealing of thermoelectric CuFe<sub>0.98</sub>Sn<sub>0.02</sub>O<sub>2</sub> films produced by powder aerosol deposition method. *Adv. Mater. Interfaces.* 2020;7:2001114. <https://doi.org/10.1002/admi.202001114>
- Stöcker T, Exner J, Schubert M, Streibl M, Moos R. Influence of oxygen partial pressure during processing on the thermoelectric properties of aerosol-deposited CuFeO<sub>2</sub>. *Materials* 2016;9:227.
- Amrute AP, Łodziana Z, Mondelli C, Krumeich F, Pérez-Ramírez J. Solid-state chemistry of cuprous delafossites: synthesis and stability aspects. *Chem. Mater.* 2013;25:4423–35. <https://doi.org/10.1021/cm402902m>
- Exner J & Moos R. Ermittlung spezifischer Materialkennwerte von Schichten mittels Interdigital-elektroden. In: Conference Publication - 12. Dresdner Sensor-Symposium; 7 Dec 2015; Dresden, Germany.
- Bernhard F. *Handbuch der technischen temperaturmessung.* Berlin, Germany: Springer; 2014.
- Tauc J. Optical properties and electronic structure of amorphous Ge and Si. *Mat. Res. Bull.* 1968;3:37–46.
- Deng Z, Fang X, Wu S, Wang S, Dong W, Shao J, et al. The effect of oxygen partial pressure on the properties of CuFeO<sub>2</sub> thin films prepared by RF sputtering. *Vacuum* 2015;115:1–5.

32. Ong KP, Bai K, Blaha P, Wu P. Electronic structure and optical properties of  $AFeO_2$  ( $A = Ag, Cu$ ) within GGA calculations. *Chem. Mater.* 2007;19:634–40. <https://doi.org/10.1021/cm062481c>
33. Vojkovic S, Fernandez J, Elgueta S, Vega FE, Rojas SD, Wheatley RA, et al. Band gap determination in multi-band-gap  $CuFeO_2$  delafossite epitaxial thin film by photoconductivity. *SN Appl. Sci.* 2019;1. <https://doi.org/10.1007/s42452-019-1387-2>
34. Xu H, Wu R, Zhang J-Y, Han W, Chen L, Liang X, et al. Revealing the electronic structure and optical properties of  $CuFeO_2$  as a p-type oxide semiconductor. *ACS Appl. Electron. Mater.* 2021;3:1834–41. <https://doi.org/10.1021/acsaelm.1c00090>
35. Kodigala SR.  $Cu(In_{1-x}Ga_x)Se_2$  based thin film solar cells. Cambridge, MA: Academic Press; 2010. eBook ISBN: 9780080920320.
36. Stöcker T, Moos R. Effect of oxygen partial pressure on the phase stability of copper-iron delafossites at elevated temperatures. *Materials* 2018;11:1888.
37. Wheatley RA, Roble M, Gence L, Acuña C, Rojas-Aedo R, Hidalgo-Rojas D, et al. Structural, optoelectronic and photothermoelectric properties of crystalline alloy  $CuAl_xFe_{1-x}O_2$  delafossite oxide materials. *J. Alloys Compd.* 2021;857:157613. <https://doi.org/10.1016/j.jallcom.2020.157613>

**How to cite this article:** Nazarenus T, Schlesier K, Biberger S, Exner J, Kita J, Köhler A, et al. Posttreatment of powder aerosol deposited oxide ceramic films by high power LED. *Int J Appl Ceram Technol.* 2022;19:1540–1553. <https://doi.org/10.1111/ijac.13977>